Materialia xxx (2018) xxx-xxx

Contents lists available at ScienceDirect

Materialia

journal homepage: www.elsevier.com

Effect of Mn and cooling rates on α-, β- and δ-Al–Fe–Si intermetallic phase formation in a secondary Al–Si alloy

H. Becker[a, c], T. Bergh[b], P.E. Vullum[b], A. Leineweber[a, *], Y. Li[c]

[a] TU Bergakademie Freiberg, Institute of Materials Science, Gustav-Zeuner-Straße 5, 09599, Freiberg, Germany
[b] Norwegian University of Science and Technology, Department of Physics, Høgskoleringen 5, Realfagbygget D5-170, NO-7491, Trondheim, Norway
[c] Norwegian University of Science and Technology, Department of Materials Science and Engineering, Alfred Getz vei 2, Bergbygget E-133, NO-7491, Trondheim, Norway

ARTICLE INFO

Keywords:
Al–Si alloys
Intermetallic phases
Microstructure formation
Solidification
Kinetics

ABSTRACT

Secondary Al–Si alloys Al7.1Si(1.5-x_{Mn})Fe(x_{Mn})Mn with x_{Mn} = 0, 0.3, 0.375, 0.6, 0.75 at.% have been solidified with different cooling rates: 0.05 K/s, 1.4 K/s, 11.4 K/s and 200 K/s. In the ternary alloy with x_{Mn} = 0 at.%, formation of the primary α_h phase is suppressed upon higher cooling rates at the cost of formation of plate-shaped β and δ phase particles. In the quaternary alloys, with increasing Mn content, α_c-phase particles with Chinese-script morphology form and replace the plate-shaped intermetallic particles. While the α_c phase forms at intermediate cooling rates only, plate-shaped particles additionally form at low and high cooling rates. The β phase dominates after solidification with lower cooling rates and the δ phase dominates upon higher cooling rates in the plate-shaped particles. The kinetic effect in terms of solidification rate and the chemical composition effect on the phase selection of Fe-containing intermetallic particles in the alloys along the solidification path have been discussed.

1. Introduction

Al–Si cast alloys are of vast technological importance especially in aerospace and automotive industries [1]. In terms of circular economy, the use of secondary Al–Si alloys is of specific interest. The production of secondary Al alloys consumes only approx. 5% of the energy required to produce primary Al [2]. However, Fe enriches in secondary, i.e. recycled, Al–Si alloys during the recycling process [3]. The presence of Fe can lead to the formation of so-called sludge which consists of large intermetallic particles solidified prior to grains of the (Al)-solid solution. For simplicity, these particles are all termed as *primary* particles, e.g. large plate-shaped β-Al–Si–Fe phase particles or huge polyhedral intermetallic α_h- or α_c-Al–Fe–Si phase particles. Such primary particles have undesired effects on the casting process [4–10] and mechanical properties of the final castings [11–14]. Additionally, intermetallic particles form after the onset of Al-solidification. To deal with Fe impurity, much effort has been spent on optimizing the microstructure in order to tailor the properties of secondary Al–Si alloys for a wide range of applications without degradation of properties.

Therefore, with the aim to avoid sludge formation and to promote the formation of intermetallic phases with less harmful morphology, e.g. the α_c phase in Chinese-script morphology, instead of the plate-shaped particles, Mn is often added and/or high cooling rates are applied [8,11–13,15–21]. The ratio of the molar fractions x of Mn and Fe in the alloy, x_{Mn}: x_{Fe}, has to be optimized to avoid a significant increase of the overall intermetallic phase fraction while achieving the intended change of intermetallic morphology [13,22,23]. Most often a ratio of 1:2 is suggested [24,13], but it has also been reported that the plates cannot be completely suppressed even at x_{Mn}: x_{Fe} = 2:1 [13]. Additionally, the optimum ratio has been reported to be dependent of the cooling rate [25] and the Si content in the alloy [13]. Depending on the casting technique, the cooling rates range from 1 to 10 K/s in permanent mold casting to 10–100 K/s in high-pressure die casting [26]. Although some studies have analyzed the growth behavior and morphology of the plate-shaped particles in specific secondary Al–Si alloys [9,13,21,2–30], a systematic approach to understand the formation or suppression of plate-shaped particles is not available.

According to the equilibrium Al–Fe–Si phase diagram [31–35], the intermetallic Al–Si–Fe phases neighboring the phase field of the (Al)-

* Corresponding author.
Email addresses: hanka.becker@iww.tu-freiberg.de (H. Becker); tina.bergh@ntnu.no (T. Bergh); PerErik.Vullum@sintef.no (P.E. Vullum); Andreas.Leineweber@iww.tu-freiberg.de (A. Leineweber); yanjun.li@ntnu.no (Y. Li)

https://doi.org/10.1016/j.mtla.2018.100198
Received 7 December 2018; Accepted 16 December 2018
Available online xxx
2589-1529/

solid solution are the hexagonal α_h-$Al_{7.1}Fe_2Si$ phase [36] and the β-$Al_{4.5}$FeSi phase [37–40]. An overview about the intermetallic phases is presented in Table 1. In presence of small amounts of Mn, e.g. 0.3 wt.%, the cubic α_c-$Al_{15}(Fe,Mn)_3Si_2$ [39,41,42] phase forms instead of the α_h phase. According to the liquidus projection [31–35], the compositional areas of primary crystallization of the α_h, the α_c and the β phase are relevant for Al–Si alloys with hypoeutectic Si contents (approx. $x_{Si} < 12$ at.%). The δ-Al_3FeSi_2 phase [39,43,44], crystallizes primarily at hypereutectic Si contents and should not be present simultaneously with the (Al)-solid solution and Si during equilibrium solidification or in an equilibrium solid state. Therefore, the δ phase is not expected to form in hypoeutectic secondary Al–Si alloys during near-equilibrium or Scheil solidification.

However, plate-shaped δ-phase particles have occasionally been reported to form in secondary hypoeutectic Al–Si alloys instead of plate-shaped β-phase particles [27,45–47]. That is the case for high cooling rates [45] or high Si contents (although still hypoeutectic) [46,47], while the effect of presence of Mn on the δ phase formation is unknown. The solidification path in hypoeutectic Al–Si alloys has been studied for a wide range of Si, Fe and Mn contents and/or cooling rates [8,16,48]. Although, some studies pointed out the importance of kinetics [16,25], the role of the δ phase in the solidification path and its microstructural characteristics have not been considered so far.

The appearance of the δ phase as plate-shaped particles similar to the β phase makes it difficult to reliably distinguish the β and the δ phase by their morphologies and the actual presence of β and/or δ phase might be overlooked, as emphasized previously by [46]. Both the β and the δ phase appear with similar Fe contents and approx. similar total (Al + Si) molar fractions, but there is a lower Si and a higher Al content in the β than in the δ phase. Often the plate-shaped particles appear very narrow in shape and are locally associated with the Al–Si eutectic region, which makes identification of the two phases by chemical composition measurement using energy dispersive X-ray spectroscopy (EDS) or wavelength dispersive X-ray spectroscopy (WDS) analysis challenging [13,47]. Nevertheless, the β and δ phase can be reliably distinguished based on their crystal structures, despite of their similarity. Both phases consist of the same types of layers, which are made up of bicapped antiprisms with Fe in the center and Al and Si at the corners. In the δ phase all cap atoms in the bicapped antiprisms are condensed [43], while in the β phase only alternate cap atoms are condensed forming double layers [37]. These successive double layers in the β phase are shifted by **a**/2 or **b**/2 displacements that can appear in disordered or in ordered sequences, leading to polytype formation. **a** and **b** are the in-plane translation basis vectors of the double layer. An elaborate description of the crystal structures of the β and the δ phase can be found in a related study [49]. Additionally, severe intergrowth of the β and the δ phase within a plate-shaped particle was encountered [49]. Consequently, correct identification of the phases present within the plate-shaped particles requires careful choice of analytical method, including access to crystallographic information data. This data must be evaluated based on knowledge of the crystal structures of the β and δ phases, including their typical polytypes and defect structures.

The present study addresses the intermetallic phase formation in Fe- and Mn-containing secondary Al–Si model alloys during solidification at different cooling rates. A thorough analysis of intermetallic phases in correlation with their microstructural appearance is carried out to access the solidification path and formation conditions of the intermetallic phases. The α_h, the α_c, the β and the δ phase are included in the analysis and discussion while the β and the δ phase are specifically in focus within the present study. These findings provide new insight into the microstructure formation under non-equilibrium solidification conditions in presence of Fe and Mn in secondary hypoeutectic Al–Si alloys. The schematic understanding of the solidification path provides a general basis for optimizing the microstructure in Fe- and Mn-containing hypoeutectic secondary Al–Si alloys.

Table 1
Summary of primary intermetallic phases forming in hypoeutectic Al–Si alloys containg Mn and Fe and their characteristics regarding morphology, crystal structure and homogeneity range.

Phase	Morphology	Crystal structure	Homogeneity range	Ref
α_h-$Al_{7.1}Fe_2Si$	Coarse polyhedral	$P6_3/mmc$	Narrow homogeneity range, Relative solubility of Mn: $Fe_{0.97}Mn_{0.03}$	[36,50]
α_c-$Al_{15}(Fe,Mn)_3Si_2$	Coarse polyhedral, coarse dendritic, Chinese-script	$Im\bar{3}$	Homogeneity range of Si and (Fe,Mn): Si: 7.4–14 at.% Fe, Mn: 15–19.2 at.% Relative solubilties of Fe and Mn: $Fe_{0.97}Mn_{0.03}$ to Fe_0Mn_1	[39,41,42,51]
β-$Al_{4.5}$FeSi	Plate-shaped	$A12/a1$, $I4_1/acd$	Relative solubility of Mn: $Fe_{0.84}Mn_{0.16}$[a]	[37,46,49]
δ-Al_3FeSi_2	Plate-shaped	$I4/mcm$	Relative solubility of Mn: $Fe_{0.79}Mn_{0.21}$	[39,43,44,46]

[a] Solubility accessed in the present paper (see Table 4).

2. Methods

2.1. Preparation and heat treatment of the alloys

Al7.1Si(1.5-x_{Mn})Fe(x_{Mn})Mn alloys with molar fractions x_{Mn} = 0, 0.3, 0.375, 0.6, 0.75 at.% and $x_{Fe} = 1.5\text{-}x_{Mn}$ representing secondary Al–Si model alloys were prepared, covering the $x_{Mn}/(x_{Fe} + x_{Mn})$ ratio from 0 to 0.5 (x_{Mn}: x_{Fe} ratio from 0 to 1:1). The alloys were melted in an electric arc furnace from Fe (AlfaAesar, pieces, 99.99% metals basis) and Al (AlfaAesar, slugs, 99.9999% metals basis), Si (AlfaAesar, pieces, 99.9999% metal basis) and Mn (AlfaAesar, pieces, 99.95% metal basis). Weighing of the ingots indicated a weight loss < 0.05%. Hence, the weighted-in alloy compositions are adopted for all original alloys.

Pieces of the material from the ingots were subjected to further heat treatment. The alloys were melted in Al_2O_3 crucibles (GTS - Gieß-Technische-Sonderkeramik GmbH & KG, 99.7%) which were encapsulated in fused silica tubes with argon atmosphere of normal pressure at maximum heat-treatment temperature (270 mbar at ambient temperature). The temperature during the whole heat treatment process was monitored by the use of a thermocouple placed adjacent to the samples. The samples were fully melted at 850 °C for 1 h. Subsequently, cooling rates were varied by different environmental cooling conditions leading to an exponential decrease of the temperature. Discontinuities during decrease of the temperature were not resolved by the temperature measurement. For comparison cooling rates at 650 °C were derived from the cooling curves (Table 2).

Table 2
Cooling rates of the Al-alloy melts starting from 850 °C melt temperature for different environmental cooling conditions. The cooling rates at 650 °C were derived from the continuously recorded cooling curves.

Environmental cooling condition	Cooling rate [K/s]	Breaking of capsules
Furnace	0.05	No
Air	1.4	No
Water	11.4	No
Water	200	Immediate

2.2. Microstructure analysis

Microstructural investigations by scanning electron microscopy (SEM) including energy-dispersive X-ray spectrometry (EDS) and electron backscatter diffraction (EBSD) were carried out on polished (final stage: colloidal silica suspension; OP-S, Struers) cross sections of the solidified alloys. A low-vacuum thermal field-emission gun (FEG), Zeiss Supra 55 Variable Pressure SEM, equipped with a Genesis EDS system and TEAM software (EDAX), was used. Backscatter electron (BSE) images were used to quantify volume fractions of intermetallic particles with plate-shaped and Chinese-script morphology. To determine average chemical compositions and the standard deviation, 6–10 EDS point measurements per phase were performed. A FEG Zeiss LEO 1530 GEMINI equipped with a Nordlys II EBSD detector (Oxford Instruments) and HKL Channel5 software (Oxford instruments) was used for single EBSD pattern acquisition for the purpose of phase identification.

Thin lamellae specimens were prepared exemplarily by focused ion beam preparation from the plate-shaped intermetallic particles in the Al7.1Si1.2Fe0.3Mn alloy for investigations by transmission electron microscopy (TEM). The utilized TEM techniques included selected area electron diffraction (SAED) and high angle annular dark field (HAADF) scanning transmission electron microscopy (STEM) imaging, in order to derive local insight into the microstructure of the β and the δ phase in plate-shaped intermetallic particles. A double C_S-aberration corrected cold FEG JEM-ARM200F (JEOL, Japan) was utilized.

An aqueous solution of NaOH (10 g NaOH per 100 ml distilled water) was used to dissolve the Al matrix (20 min) and extract intermetallic particles into intermetallic powders. Powder X-ray diffraction (P-XRD) was carried out to determine the relative phase fraction within the plate-shaped intermetallic particles. A Bruker D8 Focus diffractometer equipped with a LynxEye™ SuperSpeed Detector was employed, working in Bragg-Brentano reflection geometry and using Cu radiation. A small amount of the powder was sedimented on 510-cut Si "zero background" sample holders. Due to the strong anisotropic morphology, the plate-shaped intermetallic particles settle with their plate plane parallel to the surface of the sample holder, resulting in strong preferred crystallographic orientation present in the P-XRD data. Therefore, the relative phase fraction of the β and the δ phase are determined from the relative integral intensities of the $\{004\}_\beta$ and $\{002\}_\delta$ peaks. This approach is justified here because the β and the δ phase appear with plate-shaped morphology, can be associated within the same plate-shaped particles and, therefore, provide very similar texture effects, have approx. the same structure factors, consequently leading to reasonable trends for the relative phase fraction of the β and the δ phase. Conversion from mass to volume fraction was taken into account.

2.3. Thermodynamic calculations using the CALPHAD method

Thermodynamic calculations by the CALPHAD method [52] using the TCAl4 database [53] within the ThermoCalc software [54] were performed to illustrate the liquidus projection and an isothermal section at 575 °C of the ternary Al–Fe–Si system in the Al-rich corner. Based on the TCAl4 database [53] the total intermetallic phase fractions after solidification for the present alloy compositions were estimated. Calculations for Scheil solidification conditions and under equilibrium conditions did not show a pronounced difference in the total intermetallic phase fractions. However, the relative phase composition of the total intermetallic phase fraction is remarkably different. Detailed evaluation of solidification paths calculated based on thermodynamic databases in comparison to experimentally derived solidification paths are not within the scope of the present study.

3. Results

3.1. General appearance of the microstructure after solidification

The microstructure of the solidified Al–Si alloy contains intermetallic phases with different morphologies and phase fractions depending on the alloy composition and on the cooling rate (Fig. 1). Note the change of magnification in Fig. 1 due to a strongly cooling-rate dependent size of the intermetallic particles. The different morphology of intermetallic particles is highlighted in Fig. 1. If coarse α_h or α_c phase particles have formed, they frequently occur at the edge of the corresponding sample.

Plate-shaped β and/or δ phase particles tend to form at low and also at high cooling rates. With increasing $x_{Mn}/(x_{Mn} + x_{Fe})$ ratio, at an increasing range of intermediate cooling rates, Chinese-script α_c-phase particles form. Details of characterization of the intermetallic particle in terms of phase identification, morphology, chemical composition and phase fraction measurements are presented in the following sections.

As shown in Fig. 1 the size of the Al dendrites decreases and the morphology of eutectic Si changes from flake-like morphology at cooling rates of 0.05 K/s, 1.4 K/s and 11.4 K/s to a fine fibrous morphology under a cooling rate of 200 K/s.

3.2. The α_h and the α_c phase

3.2.1. Occurrence depending on Mn content and cooling rate

The hexagonal α_h phase is observed in the Mn-free ternary Al–Si–Fe alloy, while the cubic α_c phase forms in Mn-containing alloys, as revealed by EBSD point measurements (Fig. 2).

Primary coarse α_h phase particles tend to form at the sample edges of the Mn-free ternary alloys cooled with 0.05 K/s (Fig. 1). The particles have diameters of approx. 500 μm and are surrounded by a layer of the β phase. The faster cooled samples appear free of α_h phase. Instead plate-shaped intermetallic particles have formed (see Section 3.3).

In the Mn-containing alloys, the α_c phase is present (Fig. 1). In the 0.05 K/s-cooled sample, primary α_c phase forms as coarse polyhedral particles at the edges of the samples with diameters of approx. 250 μm. In the 1.4 K/s- and 11.4 K/s-cooled samples, the primary α_c phase has coarse facetted dendritic to hollow-polyhedron shape. In the bulk region in 0.05 K/s-, 1.4 K/s- and 11.4 K/s-cooled samples, the α_c phase additionally solidifies in variations of Chinese-script morphology within the bulk of the samples. The α_c phase with Chinese-script morphology is located within the Al dendrites, but not within the Al–Si eutectic region. In 200 K/s-quenched alloys, no primary intermetallic phase has formed. In alloys with x_{Mn} = 0.3 at.% and 0.375 at.%, no α_c phase is present. In alloys with x_{Mn} = 0.6 at.% and 0.75 at.%, the α_c phase formed in Chinese-script morphology located within the Al–Si eutectic region.

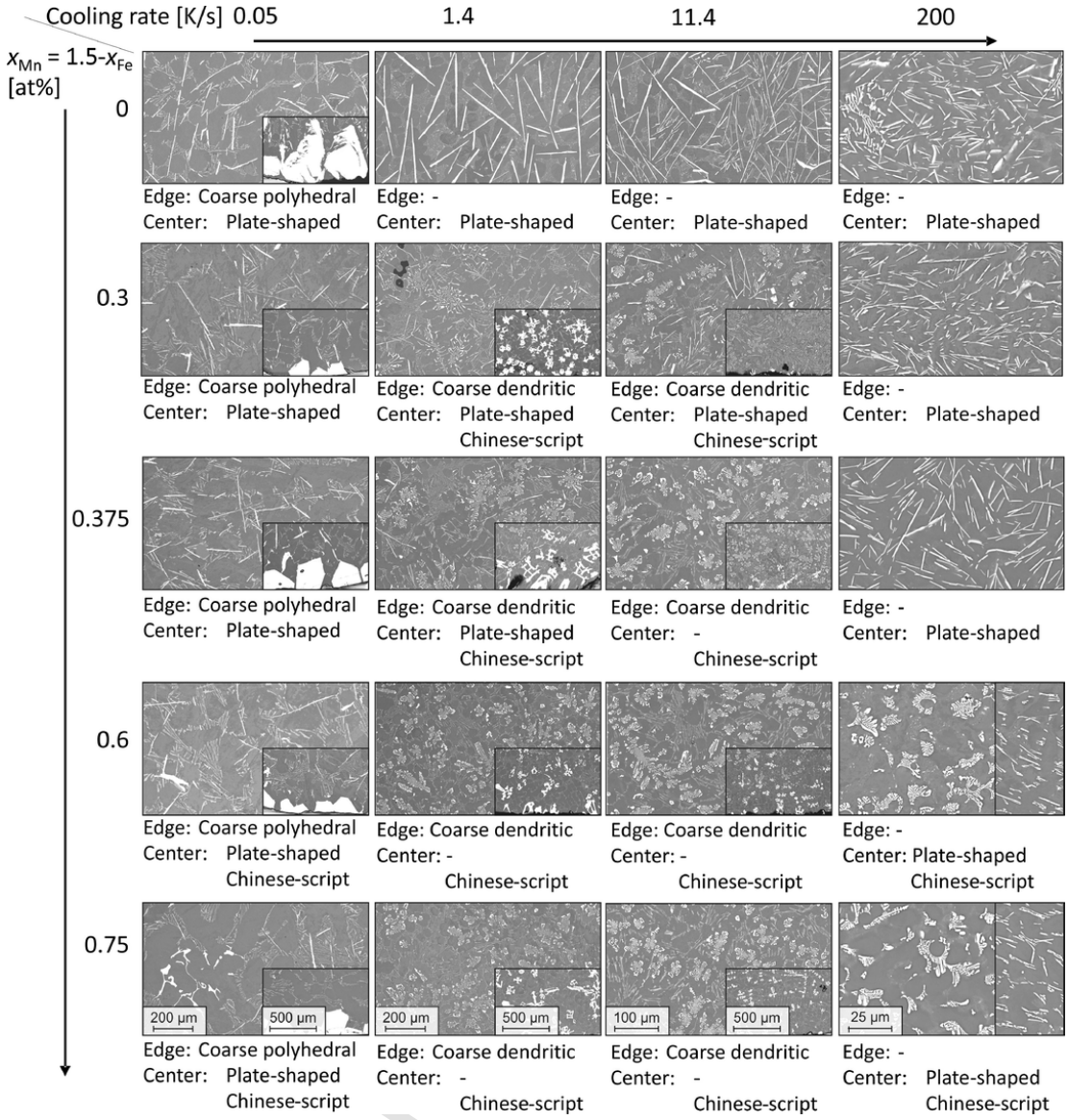

Fig. 1. SEM images in BSE contrast showing the evolution of the microstructure of the Al7.1Si(1.5-x_{Mn})Fe(x_{Mn})Mn alloys depending on the Fe and Mn contents and the cooling rate. The images correspond to the bulk of the solidified material, while the insets show the primary particles located at the edge of the samples. The insets for x_{Mn} = 0.6, 0.75 at.% and 200 K/s with the same magnification illustrate the presence of colonies of plate-shaped particles next to the predominant microstructure in the samples. The intermetallic phases appear white, Si in light gray and Al in gray, pores in black. Plate-shaped intermetallic particles belong to the β and/or the δ phase. Particles with coarse polyhedral, coarse dendritic or Chinese-script morphology are identified as the α_h phase in alloys with x_{Mn} = 0 at.% and as the α_c phase in alloys with x_{Mn} > 0.3 at.%. Note the change of the magnification in dependence on the cooling rate.

3.2.2. Chemical composition

EDS point measurements reveal that the α_h phase has a x_{Fe} content higher than the total transition metal content $x_{Fe} + x_{Mn}$ in the α_c phase. A superficial phase identification of the α_h and α_c phase might be the origin of the reported experimental homogeneity range of the α_h phase, which is illustrated in Fig. 3. The $x_{Mn}/(x_{Mn} + x_{Fe})$ ratio in the α_c phase increases with increasing Mn content in the alloy and is accompanied by an increase in the Si content. The chemical composition of the α_c phase in coarse polyhedral and Chinese-script morphology differs, as observed previously in [55]. This α_c phase in Chinese-script morphology shows higher Si contents and lower $x_{Mn}/(x_{Mn} + x_{Fe})$ ratios than the coarse polyhedral α_c particles. This is illustrated in Fig. 3. An increasing cooling rate leads to a decreasing $x_{Mn}/(x_{Mn} + x_{Fe})$ ratio in the coarse polyhedral and coarse dendritic particles and an increasing ratio in the Chinese-script particles. For reference reasons the chemical compositions of the α_h and the α_c phase are compiled in Table A1 in the appendix. The chemical composition of the Chinese-script particles in the 200 K/s-quenched alloys were not measured because their size was too small to be resolved by EDS in SEM.

3.3. The β and the δ phase in plate-shaped particles

3.3.1. Occurrence of plate-shaped particles depending on Mn content and cooling rate

Plate-shaped particles are observed in all alloys cooled with 0.05 K/s, where these occur within the Al–Si eutectic regions and, therefore, have not formed as primary phase. The length of the plates in 2D cross sections ranges between 60 and 80 µm. The broad distribution of the plate length in 2D cross sections manifests in standard deviations of approx. 2/3 of the average value (Table 3).

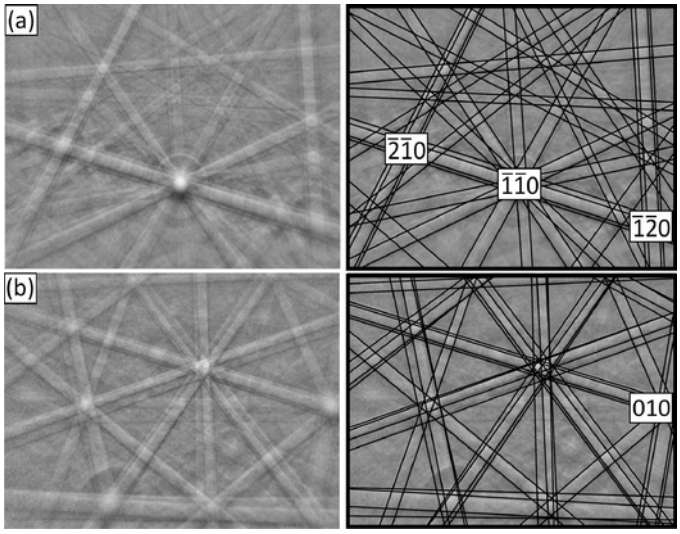

Fig. 2. Exemplary EBSD pattern from (a) a coarse polyhedral particle identified as the α_h phase in alloys with $x_{Mn} = 0$ at.% and (b) coarse polyhedral particles, coarse dendrites and Chinese-script particles identified as the α_c phase in Mn-containing alloys (e.g. $x_{Mn} = 0.3$ at.%). Raw EBSD patterns are shown on the left side, and the EBSD patterns with the superposed solution are shown on the right side.

In the Mn-free ternary Al–Si–Fe alloy cooled with 1.4 K/s and 11.4 K/s, plate-shaped particles have formed as primary phase being located within the Al dendrites. Without the presence of the primary α_h phase and cooling rate of 1.4 K/s, the average plate length is approx. 200 μm, and this length decreases with increasing cooling rate.

In the Mn-containing alloy, plate-shaped particles have formed next to Chinese-script α_c phase. With increasing Mn content a range of intermediate cooling rates exists for which plate-shaped particles do not form next to Chinese-script α_c-phase particles. The average plate length after cooling with 1.4 K/s of the alloy with $x_{Mn} = 0.3$ at.% is approx. 50 μm and decreases with increasing cooling rate and Mn content to 20 μm.

After quenching with 200 K/s, plate-shaped intermetallic particles have formed in alloys with $x_{Mn} = 0$, 0.3 at.% and 0.375 at.%, while colonies of plates can be observed next to the α_c phase in Chinese-script morphology in alloys with $x_{Mn} = 0.6$ at.% and 0.75 at.%. In contrast to the slower cooling rates, the plate-shaped intermetallic particles occur within the Al–Si eutectic region after quenching with 200 K/s and their size is < 10 μm.

3.3.2. Simultaneous presence of the β and the δ phase in plate-shaped particles

A fraction of the plate-shaped particles exhibits stripes in dark and light gray contrast upon SEM imaging with BSE, which can be attributed to the simultaneous occurrence of the β and the δ phase in the same plate-shaped particle according to [49]. The light gray stripes occur irregularly distributed, mostly at the edges and/or sometimes in the center of the plates. This is exemplarily illustrated in Fig. 4(a–c) for the plates occurring in the alloy with $x_{Mn} = 0.3$ at.% cooled with 0.05 K/s, 1.4 K/s and 11.4 K/s.

The number fraction of plate-shaped particles containing simultaneously the β and the δ phase increases with increasing Mn content and tends to increase with increasing cooling rate (Fig. 4(d)). This aspect of plate-shaped particles in alloys quenched with 200 K/s was not evaluated because their cross sections are too narrow to get sufficient contrast differences using BSE in a SEM. Note that the number fraction of plates containing both phases is not proportional to the relative volume fraction of the two phases.

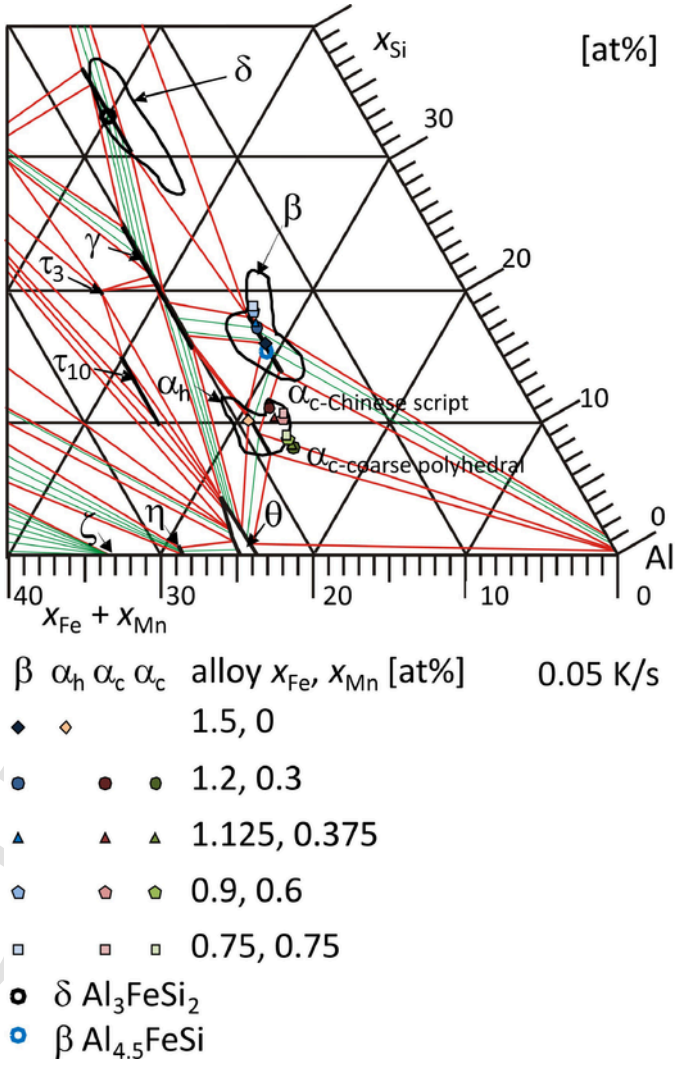

Fig. 3. Chemical composition of the β, the α_h and the α_c phase projected into the Al–Si–Fe phase diagram for the investigated alloys cooled with 0.05 K/s. Isothermal section of the Al–Fe–Si phase diagram at 575 °C calculated based on the TCAL4 database [53] using the ThermoCalc software [54]. Phase fields of β, α_h and δ from experimental phase compositions according to [32] are indicated by regions margined with black lines. .

Table 3
Length of plate-shaped particles depending on the cooling rate and the alloy composition, represented by the average and standard deviation rounded to an order of magnitude of 10 μm for 0.05 K/s-, 1.4 K/s- and 11.4 K/s-cooled samples or 1 μm for 200 K/s-quenched samples. The large standard deviations are a consequence of the broad distribution of the particle length in 2D cross sections. Empty cells refer to samples without plate-shaped particles.

Length [μm]	Cooling rate [K/s]			
Alloy	0.05	1.4	11.4	200
Al7.1Si1.5Fe	70 ± 40	200 ± 140	40 ± 50	7 ± 4
Al7.1Si1.2Fe0.3Mn	80 ± 70	50 ± 30	20 ± 20	7 ± 4
Al7.1Si1.175Fe0.375Mn	70 ± 40	40 ± 30		7 ± 4
Al7.1Si0.9Fe0.6Mn	60 ± 50			5 ± 3
Al7.1Si0.75Fe0.75Mn	60 ± 50			5 ± 3

TEM bright field imaging and a corresponding SAED pattern confirm the simultaneous existence of the β and δ phase in a plate-shaped particle in the alloy with $x_{Mn} = 0.3$ at.% (Fig. 5(a,b)). Ledges are present at the interface of the β and the δ phase, causing pronounced

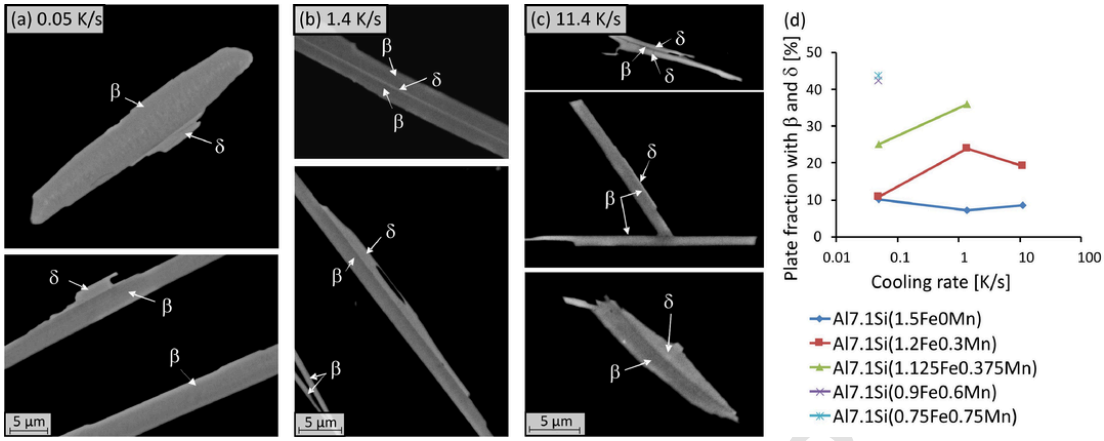

Fig. 4. Appearance of the β and the δ phase in plate-shaped intermetallic particles in the Al7.1Si1.2Fe0.3Mn alloy in SEM/BSE contrast for cooling rates (a) 0.05 K/s (b) 1.4 K/s and (c) 11.4 K/s. The Al matrix and Al–Si eutectic appear black. (d) Number fraction of plates containing the β and the δ phase depending on the cooling rate for the different alloy compositions. These aspects are not evaluated for plate-shaped particles in alloys quenched with 200 K/s because the plate-shaped particles' cross sections in these alloys are too narrow to resolve contrast differences using BSE in a SEM.

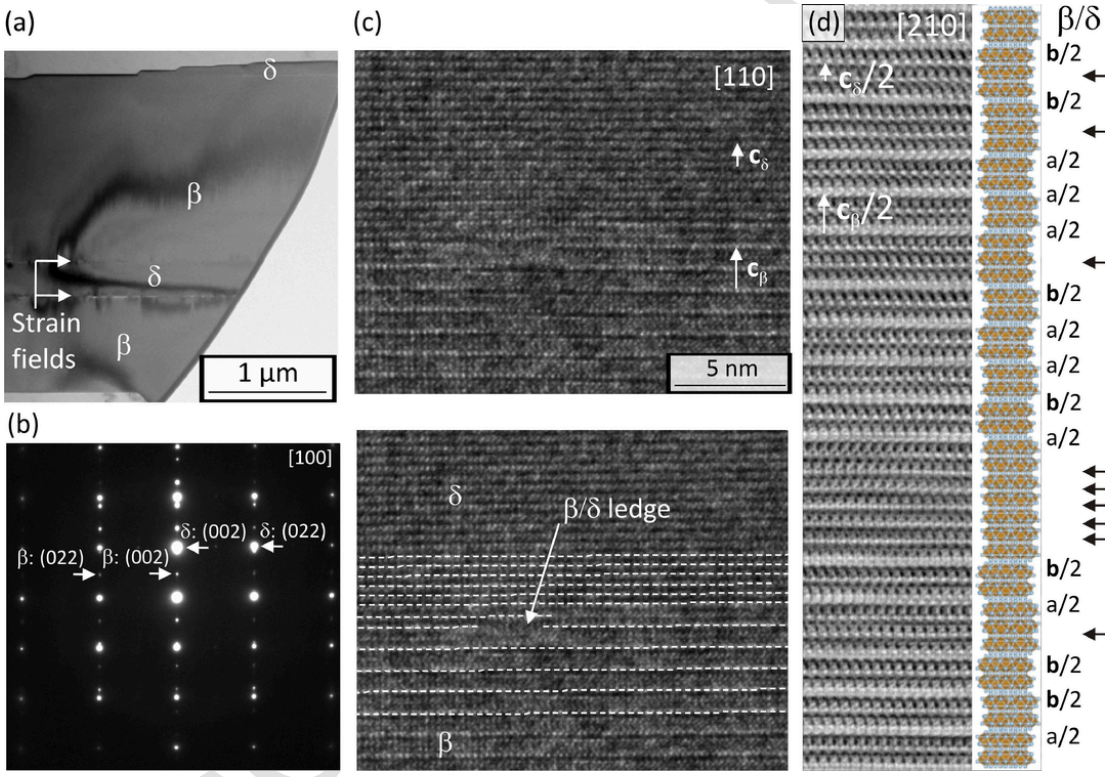

Fig. 5. (a) TEM bright field image of a lamella from a plate-shaped intermetallic particle from the Al7.1Si1.2Fe0.3Mn alloy cooled with 1.4 K/s containing extended regions of β and δ phase. Note the pronounced strain field at the β/δ interface. (b) SAED image of the β and the δ phase with [100] incidence direction corresponding to a selected area covering a β- and δ-phase region. (c) High-resolution TEM image for [110] incidence direction showing a β/δ ledge between the β and δ phase causing the strain field visible in (a) by variations in the diffraction contrast. The dashed white lines support the visibility of the β/δ ledge. (d) Fourier-filtered HAADF image with irregular β and δ stacking sequence and non-periodic stacking of double layers in β. The corresponding schematic stacking by the β and δ layers indicates the stacking sequence. **a**/2 and **b**/2 are the displacement vectors between the double layers in β. The arrows point at δ-like layer sequences. Note that, the images in (a,c), (b) and (d) are taken from three different lamellae allowing to access three different incidence direction.

strain fields (Fig. 5(a)). Such a ledge is exemplarily highlighted in Fig. 5(c). Next to the extended β- and δ-phase regions, also short δ-like stacking sequences are present within the β phase (Fig. 5(d)). The stacking sequence according to **a**/2 or **b**/2 displacements within the β phase is indicated.

3.3.3. Chemical composition

The chemical composition of the β phase was evaluated for plate-shaped particles without visible presence of the δ phase (Table 4). The stripes of the δ phase were too narrow for reliable quantitative evaluation of the chemical composition from the EDS signal. With increasing Mn content the $x_{Mn}/(x_{Mn} + x_{Fe})$ ratio increases up max. 17% of transition metal sites occupied with Mn corresponding to max. 2.3 at.% Mn in the β phase. The increase of the Mn content is accompanied by a decrease of the Fe content and significant increase of the Si content in the β phase (Fig. 3). Generally, the Si content is slightly higher and the transition metal content lower than expected according to the most often reported composition $Al_{4.5}FeSi$.

Table 4
Chemical compositions of the β phase particles. The chemical compositions of the β phase in the secondary Al–Si alloy corresponds to β plates without stripy contrasts in SEM/BSE images, i.e. without indication for the presence of the δ phase. The difference to 100 at.% is x_{Al}.

Chemical composition	Cooling			
[at.%]	Rate	x_{Si}	x_{Fe}	x_{Mn}
Alloy	[K/s]	[at.%]	[at.%]	[at.%]
Al7.1Si1.5Fe	0.05	16.1 ± 0.2	14.9 ± 0.05	0
Al7.1Si1.5Fe	1.4	14.7 ± 0.1	15.1 ± 0.1	0
Al7.1Si1.5Fe	11.4	15.0 ± 0.4	15.1 ± 0.1	0
Al7.1Si1.2Fe0.3Mn	0.05	17.5 ± 0.4	14.1 ± 0.4	0.9 ± 0.3
Al7.1Si1.2Fe0.3Mn[a]	1.4	17.8 ± 0.4	13.9 ± 0.2	0.8 ± 0.1
Al7.1Si1.2Fe0.3Mn	11.4	17.1 ± 0.9	12.7 ± 1.4	0.8 ± 0.3
Al7.1Si1.175Fe0.375Mn	0.05	17.7 ± 0.1	13.7 ± 0.1	1.0 ± 0.1
Al7.1Si1.175Fe0.375Mn	1.4	17.9 ± 0.6	13.6 ± 0.7	0.7 ± 0.1
Al7.1Si0.9Fe0.6Mn	0.05	18.9 ± 0.1	12.6 ± 0.2	2.0 ± 0.1
Al7.1Si0.75Fe0.75Mn	0.05	18.8 ± 0.4	12.2 ± 0.4	2.3 ± 0.2

[a] [49].

3.4. Evolution of phase fractions

The evolution of the volume fraction Φ according to different categories of intermetallic particles is analyzed referring to:

- the intermetallic phases β, δ, α_h, α_c as Φ_β, Φ_δ, $\Phi_{\alpha h}$, $\Phi_{\alpha c}$,
- the specific morphologies plate-shaped particles, Chinese-script particles and primary coarse polyhedral/coarse dendritic particles as Φ_{plates}, $\Phi_{Chinese\text{-}script}$, Φ_{coarse},
- the location of the intermetallic particles in the bulk of the sample and at the edge as Φ_{bulk}, Φ_{sludge}.

The total amount of intermetallic phases $\Phi_{total(ThermoCalc)}$ present in the alloys after solidification is derived from thermodynamic calculations.

The volume fractions are assessed from combined metallographic image analysis, XRD analysis and thermodynamic calculations. Φ_{bulk} is determined from metallographic image analysis and is separated into Φ_{plates} and $\Phi_{Chinese\text{-}script}$. The analysis of the P-XRD data confirms that the plate-shaped particles consist of the β and δ phase and provides integral information on the relative phase fraction of the β and δ phase. Their volume fractions, Φ_β and Φ_δ, are evaluated based on relative integral intensity analysis of $\{004\}_\beta$ and $\{002\}_\delta$ peaks in P-XRD data in combination with the volume fractions of plate-shaped particles from quantitative metallographic analysis. The P-XRD data is exemplarily shown for the ternary Al–Fe–Si alloy in Fig. 6. The relative volume fraction of Φ_β within the plate-shaped particles is summarized in Table 5.

Some relationships between the categories of volume fractions can be formulated:

- $\Phi_\alpha = \Phi_{Chinese\text{-}script} + \Phi_{coarse}$, Φ_α contains $\Phi_{Chinese\text{-}script}$ and Φ_{coarse},
- $\Phi_{coarse} \approx \Phi_{sludge}$, Φ_{coarse} can be assumed to be largely equivalent to Φ_{sludge}[1],
- $\Phi_{sludge} = \Phi_{total(ThermoCalc)} - \Phi_{bulk}$, Φ_{sludge} is estimated as the difference between $\Phi_{total(ThermoCalc)}$ and Φ_{bulk}.
- $\Phi_{bulk} = \Phi_{Chinese\text{-}script} + \Phi_{plates}$, volume fraction of all intermetallic particles present in the bulk region of the material,
- $\Phi_{plates} = \Phi_\beta + \Phi_\delta$, Φ_{plates} consist of β and δ phase.

The derived results are presented in volume fraction vs. cooling rate diagrams in Fig. 7(a–e). The phase fraction evolution of the ternary alloy and in the Mn-containing alloys is different due to the presence of different types of intermetallic phases. The hexagonal α_h phase does not evolve in Chinese-script morphology with increasing cooling rate. α_h-phase sludge particles were observed in the alloy with the lowest investigated cooling rate of 0.05 K/s only. At higher cooling rates, plate-shaped particles are present.

Replacing 0.3 at.% Fe by Mn is sufficient for the formation of the cubic α_c phase as sludge and in Chinese-script morphology. The tendency to form sludge, persists to higher cooling rates with increasing Mn content and is only fully suppressed at 200 K/min. The suppression of sludge formation goes alongside with increasing Φ_{bulk}. The entire suppression of plate-shaped intermetallic particles in favor of particles with Chinese-script morphology requires a critical Mn content between 0.3 at.% and 0.375 at.% and depends on the cooling rate. The range of cooling rates for which the formation of plate-shaped intermetallic particles is suppressed and α_c phase forms is limited towards low and high cooling rates and increases with increasing Mn content.

The plate-shaped particles are composed of the β and the δ phase. The relative phase fraction of the δ phase increases strongly with increasing cooling rate and slightly with Mn content, and vice versa for the relative phase fraction of the β phase. At a cooling rate of 0.05 K/s, the major phase in the plate-shaped particles is the β phase, while at 200 K/s the major phase is the δ phase. This is also observed when plate-shaped particles form at low and high cooling rates, but not at intermediate cooling rates.

4. Discussion

4.1. Formation and growth of the β and the δ phase in plate-shaped particles

4.1.1. Proof of the simultaneous presence of the β and the δ phase in single plate-shaped particles

The present study reveals that not only the β- and α_h- or α_c-phase formation is affected by the cooling rate and Mn content but also the formation of the δ phase plays a role in solidification and, thus, affects the microstructure formation. At low cooling rates, the β phase is the dominating phase within the plate-shaped particles. At high cooling rates, the δ phase is the dominating phase. An increasing Mn content in the alloy will give an increasing relative volume fraction of the δ phase in plate-shaped particles, at constant cooling rate (see Table 5 and Fig. 7).

The trend of increasing fraction of δ phase and decreasing fraction of β phase in plate-shaped particles confirms the observation reported in literature that the δ phase forms at comparably higher cooling rates [45]. In a ternary Al7Si0.9Fe alloy, the β phase formed at cooling rates less than 2.7 K/s and the δ phase formed between 2.7 and 4.4 K/s [45].

[1] Also primary plate-shaped particles can be part of the sludge. Sludge is usually inhomogeneously distributed in the sample, e.g. settled to the bottom of a crucible. In the present case, the large primary plate-shaped particles, e.g. in the ternary Al-Fe-Si alloy, appear evenly distributed across the whole sample and are, therefore, assigned to the bulk of the sample.

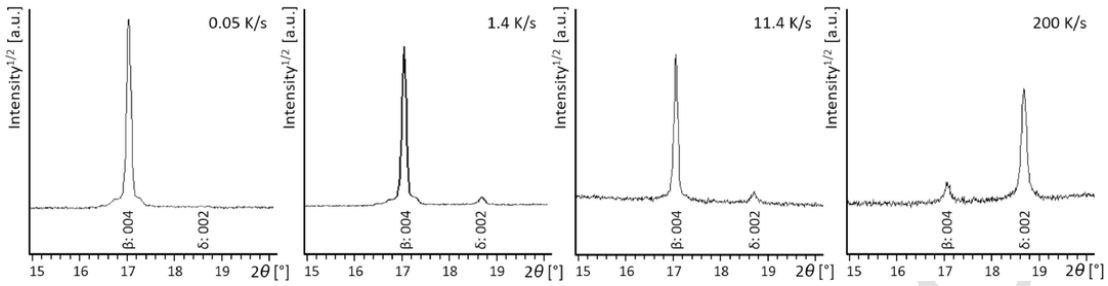

Fig. 6. P-XRD data of the intermetallic particles extracted from the Al7.1Si1.5Fe alloy cooled with different rates. The angular range 2θ from 15° to 20° is shown containing the 004 peak of the β phase and 002 peak of the δ phase used as indication for the relative phase fraction of the β and δ phase within in the plate-shaped particles.

Table 5
Relative volume fraction of the β phase within the plate-shaped particles $\Phi_\beta/(\Phi_\beta + \Phi_\delta) = \Phi_\beta/\Phi_{plates}$ as derived from evaluation of Powder-X-ray diffraction data. Empty cells refer to samples without plate-shaped particles.

Φ_β/Φ_{plates} [%]	Cooling rate [K/s]			
Alloy	0.05	1.4	11.4	200
Al7.1Si1.5Fe	100	95	93	11
Al7.1Si1.2Fe0.3Mn	97	[a]	61	8
Al7.1Si1.175Fe0.375Mn	96	72		2
Al7.1Si0.9Fe0.6Mn	92			0
Al7.1Si0.75Fe0.75Mn	87			0

[a] Intermetallic powder has not been extracted from this sample, because the sample was used for other investigations.

However, the microstructural appearance of the β and/or δ phase in plate-shaped particles had not been clearly shown until a related study [49]. There, the simultaneous presence of the β and the δ phase in plate-shaped particles is scrutinized. Previously, the simultaneous presence was concluded based on chemical composition from EDS measurements which can, however, be inconclusive for small particle sizes [47,56]. In [47] the reported Al and Si contents are higher than expected for the β phase, which was attributed to the presence of the δ phase. Though, considering the small size of the plate-shaped particles, it is likely that the EDS signal also contained information from surrounding Al–Si eutectic. An uncommented SAED pattern in Fig. 2(b) in [57] showed crystallographic evidence for presence of β and δ in a plate-shaped particle.

The present investigation (Figs. 4 and 5), as well as a related study [49] prove the simultaneous presence of the β and the δ phase in plate-shaped particles. The δ phase can occur in the form of an extended δ-phase region that can undoubtedly be identified as δ phase, and in the form of short δ-like stacking sequences within the β phase, which can be considered as a typical planar defect in the β phase.

4.1.2. Extended β- and δ-phase regions in a plate-shaped particle

In view of the solidification conditions, different formation mechanisms can be discussed to explain the simultaneous occurrence of the β and the δ phase in extended regions within the same plate-shaped particles. Potentially, these are either (1) remains of an incomplete phase transformation of δ to β of original δ plates or (2) are observed as-solidified. Both ideas are based on considering that the reaction path is different for different cooling rates caused by kinetic effects, and therefore, different microstructures evolve. At high cooling rates, nucleation or growth of one phase, as well as diffusion, can be suppressed and formation of other phases than during equilibrium solidification can occur. Consequently, a situation can be assumed for which the location of the compositional areas of primary crystallization of a phase, the *primary phase areas*, significantly differ from the primary phase areas in the equilibrium liquidus projection. Thus, also the solidification path differs. The solidification path for the Al–Fe–Si alloy and the Al–Fe–Mn–Si alloy according to calculated and deduced apparent liquidus projections are discussed in detail in Section 4.2.

Considering idea (1), it is assumed that the δ phase forms from the hypoeutectic melt during non-equilibrium solidification and subsequently transforms to β and Si [47,56] via a reaction with the sur-

Table A1
Chemical compositions of the α_h and the α_c phase in particles with polyhedral bulk and Chinese-script morphology. Difference to 100 at.% is x_{Al}.

	Cooling rate	Phase	Polyhedral bulk particles			Chinese-script particles		
			x_{Si}	x_{Fe}	x_{Mn}	x_{Si}	x_{Fe}	x_{Mn}
Alloy	[K/s]		[at.%]	[at.%]	[at.%]	[at.%]	[at.%]	[at.%]
Al7.1Si1.5Fe	0.05	α_h	10.2 ± 0.1	19.3 ± 0.1				
Al7.1Si1.2Fe0.3Mn	0.05	α_c	8.4 ± 0.1	12.4 ± 0.1	4.9 ± 0.1	11.2 ± 0.1	14.2 ± 0.1	2.9 ± 0.1
Al7.1Si1.2Fe0.3Mn	1.4	α_c	8.8 ± 0.3	12.6 ± 0.2	4.6 ± 0.1	10.6 ± 0.3	13.1 ± 0.4	3.5 ± 0.1
Al7.1Si1.2Fe0.3Mn	11.4	α_c	8.7 ± 0.5	13.1 ± 0.1	4.2 ± 0.1	10.3 ± 0.2	13.1 ± 0.4	3.8 ± 0.1
Al7.1Si1.175Fe0.375Mn	0.05	α_c	8.6 ± 0.1	11.7 ± 0.1	5.4 ± 0.1	10.3 ± 0.1	14.0 ± 0.1	3.2 ± 0.1
Al7.1Si1.175Fe0.375Mn	1.4	α_c	8.7 ± 0.2	12.1 ± 0.1	5.0 ± 0.1	10.3 ± 0.5	12.0 ± 0.3	4.7 ± 0.1
Al7.1Si1.175Fe0.375Mn	11.4	α_c	9.1 ± 0.4	12.3 ± 0.1	5.0 ± 0.1	10.0 ± 0.1	12.4 ± 0.2	4.9 ± 0.2
Al7.1Si0.9Fe0.6Mn	0.05	α_c	9.5 ± 0.4	8.7 ± 0.1	8.0 ± 0.1	10.7 ± 0.2	11.1 ± 0.1	5.5 ± 0.1
Al7.1Si0.9 Fe0.6Mn	1.4	α_c	9.8 ± 0.3	9.2 ± 0.1	7.4 ± 0.1	10.9 ± 0.3	9.5 ± 0.4	7.0 ± 0.4
Al7.1Si0.9 Fe0.6Mn	11.4	α_c	9.4 ± 0.2	10.0 ± 0.1	7.4 ± 0.1	10.5 ± 0.1	9.9 ± 0.1	7.0 ± 0.2
Al7.1Si0.75Fe0.75Mn	0.05	α_c	9.3 ± 0.1	7.8 ± 0.1	9.3 ± 0.2	10.9 ± 0.2	9.5 ± 0.3	7.4 ± 0.3
Al7.1Si0.75 Fe0.75Mn	1.4	α_c	9.5 ± 0.1	7.8 ± 0.1	9.1 ± 00.1	10.8 ± 0.2	8.9 ± 0.6	7.6 ± 0.4
Al7.1Si0.75 Fe0.75Mn	11.4	α_c	9.8 ± 0.3	7.4 ± 0.1	9.2 ± 0.1	11.8 ± 0.1	7.9 ± 0.1	8.5 ± 0.1

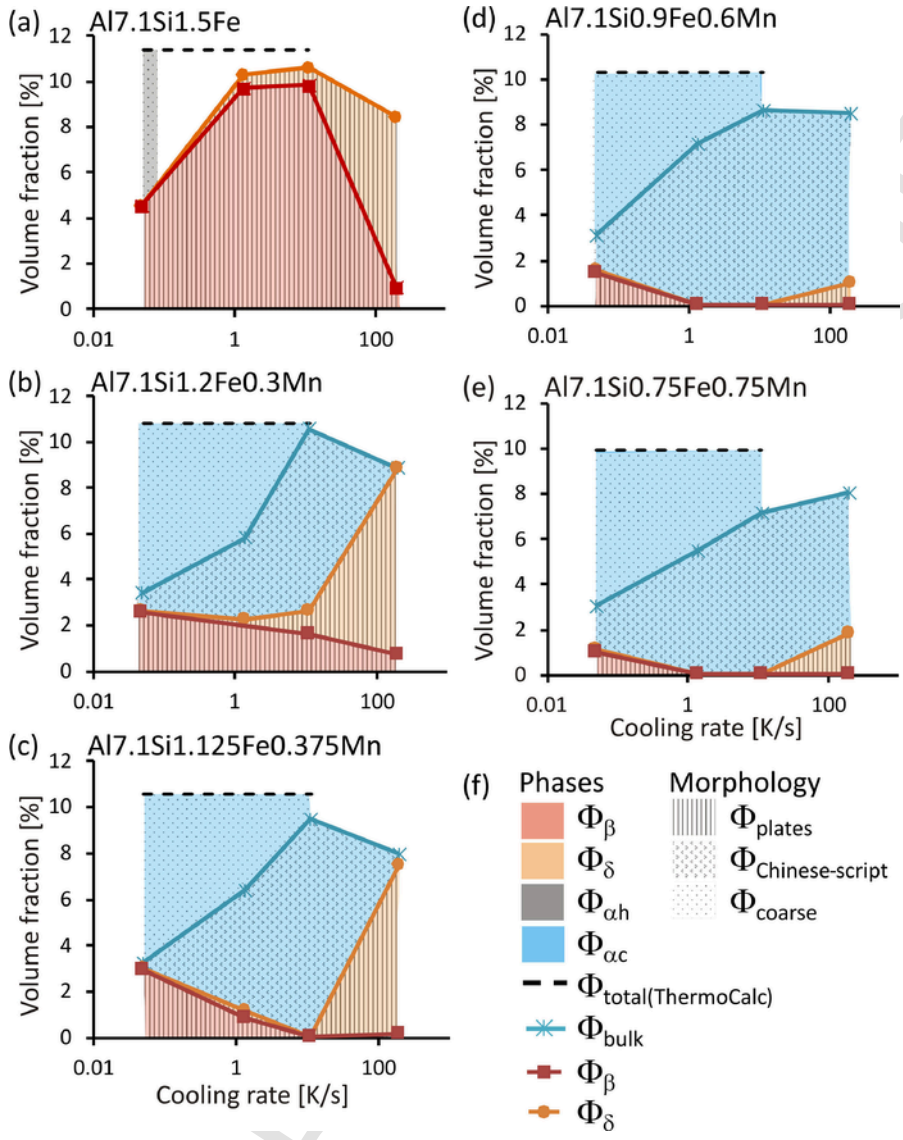

Fig. 7. Volume fractions Φ of the occurring intermetallic phases and the volume fraction of characteristic morphologies of the intermetallic phases depending on the applied cooling rates for the investigated alloys (a) Al7.1Si1.5Fe, (b) Al7.1Si1.2Fe0.3Mn, (c) Al7.1Si1.125Fe0.375Mn, (d) Al7.1Si0.9Fe0.6Mn and (e) Al7.1Si0.75Fe0.75Mn. The legend is illustrated in (f). Note that the lines and shaded areas are meant as guides to the eyes. For an explanation on the determination of the volume fractions *Φ*, see text.

rounding liquid melt [47,56] or the (Al)-solid solution [58]. If these reactions could not complete in the δ phase particles, some of the plate-shaped particles will have the δ phase in the core and the β phase on the outside [47,56]. This phase transformation would be associated with substantial diffusion [47], including precipitation of Si [58]. Assuming the most often used formulas β-$Al_{4.5}FeSi$ [37–40] and δ-Al_3FeSi_2 [39,43,44] and lattice parameters from [49] together with the lattice parameters of Si ($Fd\bar{3}m$) from [59] and of Al ($Fm\bar{3}m$) from [32], the following equation yield the chemical and volume turnover associated with formation of ½ unit cell of β phase from 1 unit cell of δ phase:

Unit cells:	1 δ-Al_3FeSi_2 +	1.5 Al	→	0.5 β-$Al_{4.5}FeSi$ +	0.5 Si
Atoms:	12Al 4Fe 8Si +	6Al	→	18Al 4Fe 4Si +	4Si
Volume:	354.1 Å^3	99.6 Å^3		395.7 Å^3	80.1 Å^3

This means after a complete transformation reaction, 83 vol% β phase should be observed with 17 vol% Si adjacent to the plate-shaped β-phase particles. When the plate-shaped particles are located within the Al–Si eutectic, it can be difficult to identify the Si from the reaction and the Si from solidification. In partially transformed particles, the according characteristic appearance would be δ phase in the center of a plate which is surrounded by β and Si. Considering that the location of δ was most often observed at the particles edge (Fig. 4), idea (1) is likely not the dominant formation mechanism for the investigated alloys and the present solidification conditions.

Considering idea (2), it is suggested that the plate-shaped particles are largely observed in the as-solidified state. According to the observed phase composition, it can be deduced that the primary phase areas of the β and the δ phase change to lower Si contents with increasing cooling rate, keeping the primary phase area of the δ phase at higher Si concentrations than that of the β phase. So, the non-equilibrium solidification starts with β-phase formation. Thus, for hypoeutectic Al–Si alloys, the Si content of the remaining melt increases during solidification along the solidification path approaching the primary phase area of the δ phase. Thus, the δ phase can solidify at the edge of the β-phase particles, as it was most often observed (Fig. 4). Due to the similarities of the crystal structures of the β and the δ phase (Fig. 5), the β phase is an excellent nucleation site for the δ phase. Additionally,

local variation of the chemical composition during solidification, e.g. towards higher Si contents, can locally lead to deviation from the overall solidification path and e.g to δ-phase formation on β-phase particles during solidification with low cooling rates. When increasing cooling rates expand the primary δ phase area to lower Si concentrations, the amount of δ phase increases with increasing cooling rate. The presence of Mn enhances this tendency.

The ledges observed at the interface between β and δ regions appear without directional relation to the edge of the plates (Fig. 5). This might indicate how β and δ are grown onto each other. The strain fields around the ledges at the β/δ interface can be attributed to the difference in the c lattice parameter $\Delta c = 100\bullet(2c_\delta - c_\beta)/c_\beta = 8.5\%$ using the lattice parameter data by [37, 43]. Additionally, a β phase double layer requires split cap atoms compared to a δ layer and the presence of an **a**/2 or **b**/2 displacement. In the case that the ledges represent a frozen state from diffusional solid-state phase transformation, the strain fields would indicate the high strain energies present during the phase transformation.

4.1.3. Short δ-like stacking sequences within the β phase

The short δ-like stacking sequences within the β phase are considered as a typical defect of the β phase. These δ-like stacking sequences can be a signature for (1) a trace from a subsequent δ to β phase transformation or (2) for an as-solidified state. In the former case (1), the presence of stackings ending in the crystal as leftovers of a diffusional phase transformation would be expected. However, the major amount of short δ-like stackings extends through the whole plate-shaped particles. In the latter case (2), mechanisms that lead to an increase of stacking faults or twins in other phases might be transferred as explanation for the origin of the δ-like stacking sequences e.g. impurity induced twinning mechanism or twin plane re-entrant edge mechanism [60,61]. Hence, the increasing fraction of δ phase (Fig. 7) and increasing probability of observation of the β and δ phase by SEM in the plate-shaped particles with increasing Mn content and increasing cooling rate (Fig. 4(d)) can be related to an increasing probability of δ-like stacking sequences which could promote the nucleation of the extended δ-phase regions. The twin-plane re-entrant edge mechanism has been used to explain the origin of twins in the β phase previously [57]. This might also be related to the observed disordered **a**/2 or **b**/2 stacking sequences or twins in the β phase (Fig. 5(d)).

Nevertheless, based on the data of the present study, the origin and role of the short δ-like stacking sequences on the presence of the δ phase or β- and δ-phase fractions in the plate-shaped particles cannot be finally resolved.

4.2. Modification of the solidification path depending on cooling rate and $x_{Mn}/(x_{Fe} + x_{Mn})$ ratio

4.2.1. The ternary alloy

In the ternary Al7.1Si1.5Fe-alloy, the primary phase forming at the slowest cooling rate of 0.05 K/s is the α_h phase, as expected for equilibrium solidification conditions [55]. Only few but very large bulk polyhedral particles have been observed indicating a low nucleation rate. With reaching the onset of solidification of the (Al)-solid solution, the α_h phase would have to completely transform into the β phase (Fig. 3). However, even during cooling with the slowest investigated cooling rate of 0.05 K/s, the α_h phase persists to room temperature corresponding to Scheil solidification characteristics. That indicates slow diffusion in the solid α_h phase to dissolve and form β phase. A fringe of β phase formed on the α_h phase which can be partially attributed to nucleation of the β phase on the α_h phase and partially to diffusional phase transformation of the α_h to the β phase. Although that represents a deviation from equilibrium solidification, the solidification path is illustrated on the liquidus surface calculated for equilibrium conditions in Fig. 8(a).

At intermediate investigated cooling rates (1.4 K/s), the α_h phase is not observed, in agreement with [55] where a cooling rate of 0.5 K/s was applied. That can be attributed to retarded nucleation of α_h as compared to the β phase [55]. Accordingly, primary β phase has developed. Small amounts of the δ phase form particularly at the outside of the β-phase plates when the melt locally enriches with Si. At high cooling rates (200 K/s), again no α_h phase forms. The plate-shaped particles mainly consist of the δ phase. These plate-shaped particles likely have formed shortly after the onset of the formation of Al dendrites.

It will be tried to rationalize the described changes in the solidification paths with increasing cooling rates in terms of *apparent liquidus projections*. Thereby, an apparent liquidus projection is depicted which complies with the observed solidification microstructure i.e. the type of phases and their location to each other e.g. occurrence of intermetallic particles within the dendrites of the (Al)-solid solution or within the eutectic region (Fig. 8(b,c)). Note that calculated liquidus projections by setting a certain phase or several phases "dormant" (i.e. excluding it/them from the thermodynamic calculations), do not comply with the observed solidification microstructure. This discrepancy can be attributed to the kinetic effects during solidification, which are not considered by the thermodynamic calculations.

A change of the morphology of the bulk α_h-phase particles or the plate-shaped particles into Chinese-script morphology was not possible in the ternary Al–Fe–Si alloy by increasing the cooling rate. The apparent liquidus projections show that a high Si content would favor the formation of the δ phase which is consistent with the observation that

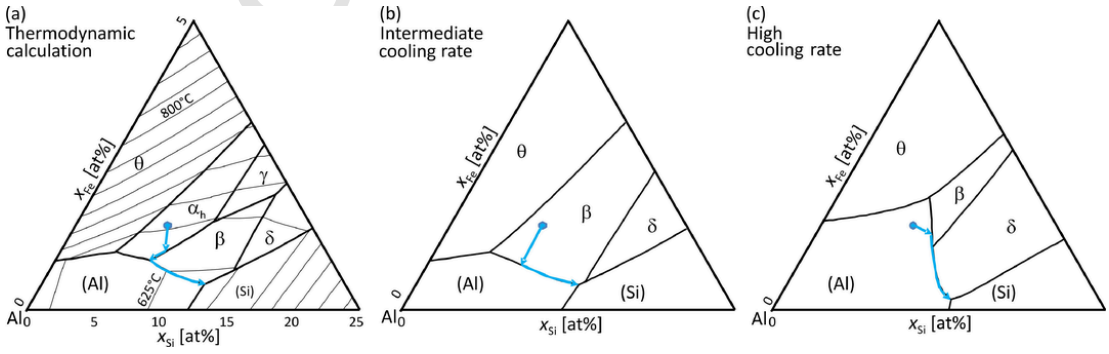

Fig. 8. (a) Liquidus projection of the Al–Si–Fe system based on thermodynamic calculations using the TCAl4 database within the ThermoCalc software and solidification path. Apparent liquidus projections for solidification conditions with (b) intermediate cooling rates and (c) high cooling rates, which comply with the solidification microstructure. Thick black lines border primary phase areas. Thin black lines in (a) indicate contour lines of the temperature in 25 °C steps. The blue circles represent the presently investigated alloy composition and blue lines schematically represent the solidification path. Note that the scales of molar fractions x_{Fe} and x_{Si} are different. Note that (b) and (c) represent apparent liquidus projections which are meant to rationalize changes in the solidification paths with increasing cooling rate. Therefore, no numbers are given at the scale.

at near-eutectic Si contents the δ phase has formed instead of the β phase alloy [46] also at intermediate to high cooling rates.

The apparent liquidus projections for $x_{Si} < 7$ wt.% and $x_{Fe} < 4.5$ wt.% for cooling rates from 1 K/s to 10 K/s shown in [62] illustrate a similar shift of the primary phase area of the β phase to lower Si contents with increasing cooling rates. The suppression of the α_h phase formation is not shown although it was not observed in the cast microstructure at high cooling rates in [62]. However, the formation of metastable Al–Fe phases is considered which is not included in the present diagrams.

4.2.2. Mn-containing alloys

The entire suppression of plate-shaped intermetallic particles in favor of α_c-phase particles with Chinese-script morphology requires a Mn content above a lower limit and depends on the cooling rate. The range of cooling rates for which the α_c phase forms only in the bulk of the alloy increases with increasing Mn content. However, next to the α_c phase with Chinese-script morphology also bulk polyhedral to coarse dendritic particles, which can settle as sludge, form.

Plate-shaped particles are observed for low cooling rates (0.05 K/s) and in the $x_{Mn}/(x_{Fe} + x_{Mn})$ range from 0 to 0.5 and for all cooling rates when $x_{Mn}/(x_{Fe} + x_{Mn})$ is 0.2. For $x_{Mn}/(x_{Fe} + x_{Mn}) = 0.25$ with cooling rate of 11.4 K/s and for $x_{Mn}/(x_{Fe} + x_{Mn}) = 0.4$ and 0.5 with cooling rate 1.4 K/s and 11.4 K/s, the formation of plate-shaped particles is suppressed. Instead the α_c phase forms. It occurs as sludge particles for cooling rates up to 11.4 K/s. With increasing Mn content, the volume fraction of primary α_c phase increases at the mentioned cooling rates. This is consistent with the increasing tendency to form sludge with increasing Mn content [23,57,63–67]. With increasing cooling rate, the morphology of the primary α_c-phase sludge particles changes from bulk polyhedral to coarse dendritic and their volume fraction decreases. Therefore, the predominant part of the intermetallic phase volume is found in the bulk of the material. Consequently, the trade-off between avoiding the formation of plate-shaped particles and increasing intermetallic phase content in bulk and/or as sludge exists not only when adding Mn [13,22,23] but also when changing the Fe:Mn ratio. For the high cooling rate (200 K/s), the plate-shaped particles consist mainly of δ phase and appear small and are located within the eutectic regions.

Liquidus projections are available for secondary Fe- and Mn-containing Al7SiCu alloys in [8,16,25,53]. Based on these and on the present experimental results, apparent liquidus projections can be deduced to illustrate the solidification path for different cooling rates, when Mn is present in the alloy (Fig. 9).

Based on this understanding, the different critical x_{Mn}: x_{Fe} ratios and cooling rates necessary to suppress the formation of the plate-shaped particles in similar alloys reported in literature can be explained. The rule of thumb for the required x_{Mn}: x_{Fe} = 1:2 ($x_{Mn}/(x_{Fe} + x_{Mn}) = 0.33$) [24] can deviate towards higher or lower Mn contents with lower or higher cooling rates. So, it is reported that even at x_{Mn}: x_{Fe} = 2:1 ($x_{Mn}/(x_{Fe} + x_{Mn}) = 0.66$) the formation of plate shaped particles may not be suppressed [13]. However, the high Si content of 9% in [13] is closer to the β and δ primary phase area.

4.3. Optimizing the microstructure

In order to achieve an optimum microstructure in secondary Al–Si alloys, a variety of parameters must be considered. The general alloy composition including the Si content and the total transition metal content, as well as the $x_{Mn}/(x_{Fe} + x_{Mn})$ ratio, determine the potentially forming phases. Essentially metastable phases were not observed in the present range of alloy compositions. The kinetic effects on the microstructure formation in secondary Al–Si alloys are pronounced. Two aims are followed by solidification with a high cooling rate: avoiding sludge formation and suppressing the formation of plate-shaped particles. Some trade-offs must be considered when the parameters are optimized.

The presence of Mn is necessary to enable the formation of the α_c phase. Thus, a lower limit of Mn content or $x_{Mn}/(x_{Fe} + x_{Mn})$ ratio is required for the suppression of plate-shaped particles towards the formation of the α_c phase in Chinese-script morphology in combination with a certain range of cooling rates. However, Mn addition increases the overall volume fraction of intermetallic phases in the bulk of the material (i.e. regions without sludge) which can counteract the positive effect of changed intermetallic phase morphology [11,14,19,22,68].

Contradictory, low cooling rates and an increasing Mn content increase the tendency to form undesirable sludge [23,55,63–67]. The sludge can potentially be removed from the metal melt [55,69,70–75]. However, if the sludge is formed, the remaining alloy composition is significantly changed due to the high partitioning of Mn in the sludge. Thus, the microstructure in the remaining material is altered [55].

At very high cooling rates, sludge formation can be fully suppressed. Nevertheless, depending on the $x_{Mn}/(x_{Fe} + x_{Mn})$ ratio, it is possible that again plate-shaped particles appear. When these appear associated with the Al–Si eutectic region, their negative effect on mechanical properties might be negligible [16,25,47], which might also be related to their comparably smaller size.

Consequently, aiming at an optimized microstructure with a low intermetallic phase fraction, without plate-shaped particles and without sludge particles, Mn should be present, the $x_{Mn}/(x_{Fe} + x_{Mn})$ ratio and total transition metal content should be as low as required and the minimum cooling rate should be chosen according to the chemical composition of the alloy. Thereby, high cooling rates seem to be generally advantageous compared to low cooling rates. Considering the alloy compositions investigated in the present study, x_{Mn} = 0.375 at.% ($x_{Mn}/(x_{Fe} + x_{Mn}) = 0.25$ and x_{Mn}: x_{Fe} = 1:3) and a cooling rate of

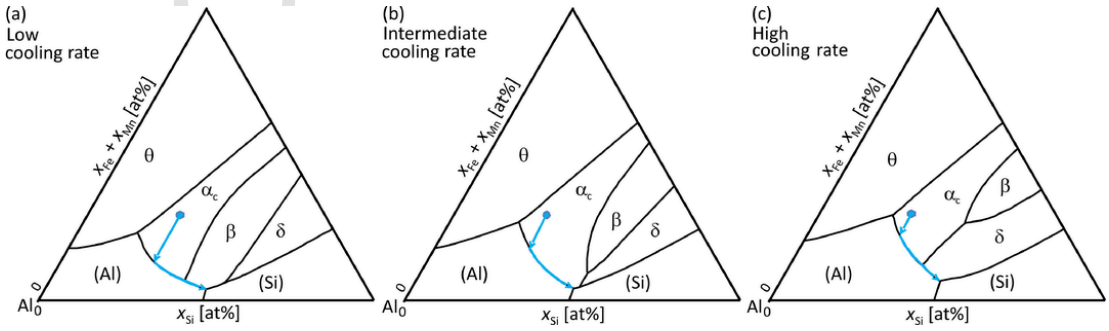

Fig. 9. Apparent liquidus projection of the Al–Si–Fe–Mn system for some fixed Mn level ($x_{Mn}/(x_{Fe} + x_{Mn})$ approx. 0.5) being compatible with the as-solidified microstructures formed under solidification conditions with (a) low cooling rates, (b) intermediate cooling rates and (c) high cooling rates, which comply with the observed solidification microstructure. The blue circles represent the presently investigated alloy composition and blue lines schematically represent the solidification path. Note that the scale of x_{Fe} and x_{Si} is different. Note that (a-c) represent apparent liquidus projections which are meant to rationalize changes in the solidification paths with increasing cooling rate. Therefore, no numbers are given at the scale.

11.4 K/s lead to a microstructure without plate-shaped particles and a small amount of sludge.

5. Conclusions

Melts of Al7.1Si(1.5-x_{Mn})Fe(x_{Mn})Mn alloys with x_{Mn} = 0, 0.3, 0.375, 0.6, 0.75 at.% and x_{Fe} = 1.5-x_{Mn} have been solidified with different cooling rates: 0.05 K/s, 1.4 K/s, 11.4 K/s and 200 K/s. The intermetallic phase particles have been analyzed in detail with focus on phase identification of plate-shaped particles.

(1) In the ternary alloy with x_{Mn} = 0, formation of the primary α_h phase is suppressed upon applying comparably high cooling rates at the cost of formation of plate-shaped particles which contain the β and/or δ phase. The β phase dominates in the plate-shaped particles after solidification with lower cooling rates while the δ phase dominates after solidification with higher cooling rates.
(2) In the quaternary alloys, Mn contents above some cooling-rate dependent value allow suppression of plate-shaped intermetallic particles in favor of α_c-phase particles with Chinese-script morphology. While the α_c phase forms at intermediate cooling rates only, it is accompanied by plate-shaped particles mainly consisting of the β phase at low cooling rates and of the δ phase at high cooling rates. An increase of the $x_{Mn}/(x_{Fe} + x_{Mn})$ ratio increases the range of intermediate cooling rates with α_c-phase formation only and is related to an increasing amount of sludge particles.
(3) Kinetic effects in combination with chemical alloy composition significantly affect the solidification path in hypoeutectic secondary Al–Si alloys. While the chemical alloy composition influences the thermodynamic properties of the phases, the kinetics additionally affect the phase formation in terms of nucleation, growth and diffusional phase transformation. Thus, the liquidus projection for different cooling rates appears significantly different compared to the equilibrium liquidus projection.
(4) Apparent liquidus projections have been suggested to allow a systematic understanding to the phase formation in the Fe- and Mn-containing secondary hypoeutectic Al–Si alloys solidified under different cooling rates.
(5) From a microstructural point of view, the phase of the plate-shaped particles cannot be reliably identified by their morphology as these particles can consist of the β and/or δ phase. This is possible due to their similar crystal structures. The observed multiphase character of the plate-shaped particles after solidification represents a nearly as-solidified state.

Declaration of interests

The authors declare that they have no known competing financial interests or personal relationships that could have appeared to influence the work reported in this paper.

Acknowledgments

This study was financially supported by the German Research Foundation in frame of the subproject A07 within the Collaborative Research Centre SFB 920. The authors are grateful for the financial support for the transmission electron microscope investigations related to activities within the center for research-based innovation SFI Manufacturing in Norway, partial funding by the Research Council of Norway under contract number 237900 and financial support by the Research Council of Norway to the NORTEM project (197405). One of the authors, H. Becker likes to thank for the financial support by the Department of Materials Science and Engineering, NTNU during her visit in Trondheim. Support by Dongdong Zhao (Department of Materials Science and Engineering, NTNU) during thermodynamic calculations and discussion of liquidus projections with Mario Kriegel (Institute of Materials Science, TU Bergakademie Freiberg) are acknowledged.

References

[1] F.C.R. Hernandez, J.M.H. Ramírez, R. Mackay, Al-Si alloys, Automotive, Aeronautical and Aerospace Applications, Springer, Cham, Switzerland, 2017239.
[2] J.A. Taylor, The Dark Side of Light Metals, Energy wasted and unnecessary CO_2 emitted as a consequence of the re-oxidation of molten aluminium, Mater. Sci. Forum 689 (2011) 429–432.
[3] L. Zhang, J. Gao, L. Nana, W. Damoah, D.G. Robertson, removal of iron from Aluminum: a review, Miner. Process. Extr. Metall. Rev. 33 (2012) 99–157.
[4] L. Lu, A.K. Dahle, Iron-rich intermetallic phases and their role in casting defect formation in hypoeutectic Al-Si Alloys, Metall. Mater. Trans. A 36 (2005) 819–835.
[5] T.O. Mbuya, B.O. Odera, S.P. Ng´ang´a, Influence of iron on castability and properties of aluminium silicon alloys: literature review, Int. J. Cast Metal. Res. 16 (2003) 451–465.
[6] X. Cao, J. Campbell, Morphology of β-Al_5FeSi Phase in Al-Si Cast Alloys, Mater. T. JIM. 47 (2006) 1303–1312.
[7] C.M. Dinnis, J.A. Taylor, A.K. Dahle, Iron-related porosity in Al–Si–(Cu) foundry alloys, Mater. Sci. Eng. A 425 (2006) 286–296.
[8] W. Khalifa, A.M. Samuel, F.H. Samuel, H.W. Doty, S. Valtierra, Metallographic observations of β-AlFeSi phase and its role in porosity formation in Al–7%Si alloys, Int. J. Cast Metal. Res. 19 (2006) 156–166.
[9] L. Liu, A.M.A. Mohamed, A.M. Samuel, F.H. Samuel, H.W. Doty, S. Valtierra, precipitation of β-Al_5FeSi phase platelets in Al-Si based casting alloys, Metall. Mater. Trans. A 40 (2009) 2457–2469.
[10] J.A. Taylor, Iron-containing intermetallic phases in Al-Si based casting alloys, Procedia Mater. Sci 1 (2012) 19–33.
[11] S. Ferraro, G. Timelli, Influence of sludge particles on the tensile properties of die-cast secondary Aluminum alloys, Metall. Mater. Trans. B 46 (2015) 1022–1034.
[12] S. Ji, W. Yang, F. Gao, D. Watson, Z. Fan, Effect of iron on the microstructure and mechanical property of Al–Mg–Si–Mn and Al–Mg–Si diecast alloys, Mater. Sci. Eng. A 564 (2013) 130–139.
[13] S. Seifeddine, S. Johansson, I.L. Svensson, The influence of cooling rate and manganese content on the β-Al_5FeSi phase formation and mechanical properties of Al–Si-based alloys, Mater. Sci. Eng. A 490 (2008) 385–390.
[14] A. Bjurenstedt, S. Seifeddine, A.E.W. Jarfors, The effects of Fe-particles on the tensile properties of Al-Si-Cu alloys, Metals 6 (2016) 1–15.
[15] A. Fabrizi, G. Timelli, The influence of cooling rate and Fe/Cr content on the evolution of Fe-rich compounds in a secondary Al-Si-Cu diecasting alloy, IOP Conf. Ser. 117 (2016) 1–6, 012017.
[16] L.A. Narayanan, F.H. Samuel, J.E. Gruzleski, Crystallization behavior of iron-containing intermetallic compounds in 319 aluminum alloy, Metall. Mater. Trans. A 25 (1994), 1761-1773.
[17] B. Kim, S. Lee, H. Yasuda, Morphological variation of the Fe/Cr-containing intermetallic phase in the Al-Si casting alloy as a function of cooling rate: time-resolved radiography, Mater. Sci. Forum 654-656 (2010) 974–977.
[18] T. Gao, Y. Wu, C. Li, X. Liu, Morphologies and growth mechanisms of α-Al(FeMn)Si in Al–Si–Fe–Mn alloy, Mater. Lett. 110 (2013) 191–194.
[19] L.B. Otani, J. Soyama, G. Zepon, A.C. e Silva, C.S. Kiminami, W.J. Botta, C. Bolfarini, Predicting the formation of intermetallic phases in the Al-Si-Fes with Mn additions, J. Phase Equlib. Diffus. 38 (2017) 298–304.
[20] W. Eidhed, Modification of β-Al_5FeSi phase compound in recycled Al-Si-Fe cast alloy by using Sr, Mg and Cr additions, J. Mater. Sci. Technol. 24 (2008) 45–47.
[21] S.K. Tang, T. Sritharan, Morphology of β-AlFeSi intermetallic in AI-7Si alloy castings, Mater. Sci. Techn. 14 (1998) 738–742.
[22] J.Y. Hwang, H.W. Doty, M.J. Kaufman, Crystallographic studies on the iron-containing intermetallic phases in the 319-type aluminium casting alloys, Philos. Mag. 88 (2008) 607–619.
[23] S.G. Shabestari, The effect of iron and manganese on the formation of intermetallic compounds in aluminum–silicon alloys, Mater. Sci. Eng. A 383 (2004) 289–298.
[24] A.M. Samuel, F.H. Samuel, H.W. Doty, Intermetallic phases in Al–Si based cast alloys: new perspective, J. Mater. Sci 31 (1996) 5529–5539.
[25] L. Bäckerud, G. Chai, J. Tamminen, Solidification Characteristics of Aluminum Alloys, Vol.2: Foundry Alloys, 2, AFS and Skanaluminium, Oslo, Norway, 1990.
[26] D. Shimosaka, S. Kumai, F. Casarotto, S. Watanabe, Effect of cooling rates during solidification of Al-5.5%Mg-2.3%Si-0.6%Mn and Al-13%Mg2Si pseudo-binary alloys on their secondary-particle morphology and tear toughness, Mater. Trans 52 (2011) 920–927.
[27] J.M. Yu, N. Wanderka, A. Rack, R. Daudin, E. Boller, H. Markötter, A. Manzoni, F. Vogel, T. Arlt, I. Manke, J. Banhart, Formation of intermetallic δ phase in Al-10Si-0.3Fe alloy investigated by in-situ 4D X-ray synchrotron tomography, Acta Mater. 129 (2017) 194–202.
[28] P. Mikolajczak, L. Ratke, Three dimensional morphology of β-Al_5FeSi intermetallics in AlSi alloys, Arch. Found. Eng. 15 (2015) 738–742.
[29] C. Puncreobutr, A.B. Phillion, J.L. Fife, P. Rockett, A.P. Horsfield, P.D. Lee, In situ quantification of the nucleation and growth of Fe-rich intermetallics during Al alloy solidification, Acta Mater. 79 (2014) 292–303.

[30] S. Terzi, J.A. Taylor, Y.H. Cho, L. Salvo, M. Suéry, E. Boller, A.K. Dahle, In situ study of nucleation and growth of the irregular α-Al/β-Al_5FeSi eutectic by 3-D synchrotron X-ray microtomography, Acta Mater. 58 (2010) 5370–5380.

[31] Y. Du, J.C. Schuster, Z.-K. Liu, R. Hu, P. Nash, W. Sun, W. Zhang, J. Wang, L. Zhang, C. Tang, Z. Zhu, S. Liu, Y. Ouyang, W. Zhang, N. Krendelsberger, A thermodynamic description of the Al-Fe-Si system over the whole composition and temperature ranges via a hybrid approach of CALPHAD and key experiments, Intermetallics 16 (2008) 554–570.

[32] G. Ghosh, Al-Fe-Si (Aluminium - Iron - Silicon), Landolt-Börnstein - Group IV Physical Chemistry 11A2, Light Metal Systems. Part 2, Springer, Berlin, Heidelberg, 2005359–409.

[33] L. Eleno, J. Vezelý, B. Sundman, M. Cieslar, J. Lacaze, Assessment of the Al corner of the ternary Al–Fe–Si system, Mater. Sci. Forum 649 (2010) 523–528.

[34] Z.-K. Liu, Y.A. Chang, Thermodynamic assessment of the Aluminum-Manganese (Al-Mn) binary phase diagram, Metall. Mater. Trans. A 30 (1999) 1081–1095.

[35] V. Raghavan, Al-Fe-Si (Aluminum-Iron-Silicon), J. Phase Equilib. 30 (2009) 184–188.

[36] J. Roger, F. Bosselet, J.C. Viala, X-rays structural analysis and thermal stability studies of the ternary compound α-AlFeSi, J. Solid State Chem. 18 (2011) 1120–1128.

[37] V. Hansen, B. Hauback, M. Sundberg, C. Rømming, J. Gjønnes, β-AlFeSi: a combined synchrotron powder diffraction, electron diffraction, high-resolution electron microscopy and single-crystal X-ray diffraction study of a faulted structure, Acta Cryst. B 54 (1998) 351–357.

[38] C. Rømming, V. Hansen, J. Gjønnes, Crystal Structure of β-$Al_{4.5}FeSi$, Acta Cryst. B 50 (1994) 307–312.

[39] G. Phragmen, On the phases occurring in alloys of aluminium with copper, magnesium, manganese, iron, and silicon, J. Inst. Metals 77 (1950) 489–552.

[40] P.J. Black, XLIX. Brillouin Zones of Some Intermetallic Compounds, Phil. Mag. 46 (1955) 401–409.

[41] M. Cooper, K. Robinson, The Crystal Structure of the Ternary Alloy α-(AlMnSi), Acta Crystallogr. 20 (1966) 614–617.

[42] M. Cooper, The Crystal Structure of the Ternary Alloy α-(AlFeSi), Acta Crystallogr. 23 (1967) 1106–1107.

[43] C. Gueneau, C. Servant, F. D'Yvoire, N. Rodier, FeAlSi, Acta Crystal. C 51 (1995) 177–179.

[44] P.I. Panday, K. Schubert, Strukturuntersuchungen in einigen Mischungen $T\text{-}B^3\text{-}B^4$ ($T = Mn,Fe,Co,Ir,Ni,Pd$; $B^a = Al,Ga,Tl$; $B^4 = Si,Ge$), J. Less-Com. Met. 18 (1969) 175–202.

[45] Y.S. Han, J.O. Choi, C.O. Choi, D.G. McCartney, Intermetallic phase formation in directionally solidified Al-Si-Fe alloy, Metals Mater. Int. 10 (2004) 27–32.

[46] M.V. Kral, P.N.H. Nakashima, D.R.G. Mitchell, Electron microscope studies of Al-Fe-Si intermetallics in an Al-11 Pct Si Alloy, Met. Mater. Trans. A 37 (2006) 1987–1997.

[47] E. Samuel, A.M. Samuel, H.W. Doty, S. Valtierra, F.H. Samuel, Intermetallic phases in Al-Si based cast alloys: new perspective, Int. J. Cast Metals Res. 27 (2013) 107–114.

[48] D. Ferdian, B. Suharno, B. Duployer, C. Tenailleau, L. Salvo, J. Lacaze, Differential thermal analysis assessment of beta phase precipitation in Al-6.5Si-1Fe alloy, Trans. Indian. Inst Met. 65 (2012) 821–825.

[49] H. Becker, T. Bergh, P.E. Vullum, A. Leineweber, Y. Li, β- and δ-Al-Fe-Si intermetallic phase, their intergrowth and polytype formation, J. Alloys Compd. ()**780**, 2019, 917-929.

[50] J.E. Tibballs, J.A. Horst, C.J. Simensen, Precipitation of α-Al(Fe,Mn)Si from the melt, J. Mater. Sci. 36 (2001) 937–941.

[51] P. Orozco-González, M. Castro-Román, J. López-Cuevas, A. Hernández-Rodríguez, R. Muñiz-Valdez, S. Luna-Álvarez, C. Ortiz-Cuellar, Effect of iron addition on the crystal structure of the α-AlFeMnSi phase formed in the quaternary Al-Fe-Mn-Si system, Rev. Metal. 47 (2011) 453–461.

[52] H.L. Lukas, S.G. Fries, B. Sundman, Computational thermodynamics, The Calphad Method, Cambridge University Press, Cambridge, 20071–324.

[53] TCAL4 - TCS Al-based alloy database, Version 4.0 http://www.thermocalc.com/media/19847/dbd_tcal40_extended_info.pdf. Assessed 25 Feb 2018.

[54] J.O. Andersson, T. Helander, L. Höglund, P.F. Shi, B. Sundman, Thermo-Calc & DICTRA, computational tools for materials science, Calphad 26 (2002) 273–312.

[55] H. Becker, A. Thum, B. Distl, M.J. Kriegel, A. Leineweber, Effect of melt conditioning on removal of Fe from secondary Al-Si alloys containing Mg, Mn and Cr, Metal. Mater. Trans. A (2018) https://doi.org/10.1007/s11661-018-4930-7.

[56] W. Khalifa, F.H. Samuel, J.E. Gruzleski, Iron intermetallic phases in the Al corner of the Al-Si-Fe system, Met. Mater. Trans. A 34 (2003) 807–825.

[57] M.H. Mulazimoglu, A. Zaluska, J.E. Gruzleski, F. Paray, electron microscope study of Al-Fe-Si intermetallics in 6021 aluminum allo, Met. Mater. Trans. A 27 (1996) 929–936.

[58] Y.S. Choi, J.S. Lee, W.T. Kim, H.Y. Ra, Solidification behavior of Al-Si-Fe alloys and phase transformation of metastable intermetallic compound by heat treatment, J. Mater. Sci. 34 (1999) 2163–2168.

[59] D.M. Toebbens, N. Stuesser, K. Knorr, H.M. Mayer, G. Lampert, E9, the new high-resolution neutron powder diffractometer at the Berlin neutron scattering center, Mater. Sci. Forum 378 (2001) 288–293.

[60] X. Liu, Y. Zhang, B. Beausir, F. Liu, C. Esling, F. Yu, X. Zhao, L. Zuo, Twin-controlled growth of eutectic Si in unmodified and Sr-modified Al–12.7%Si alloys investigated by SEM/EBSD, Acta Mater 97 (2015) 338–347.

[61] S.-Z. Lu, A. Hellawell, The mechanism of silicon modification in aluminum-silicon alloys: impurity Induced Twinning, Metal. Trans. A 18 (1987) 1721–1733.

[62] Y. Langsrud, Silicon in commercial aluminum alloys – What becomes if it curing DC-casting, Key Eng. Mater 44-45 (1990) 95–116.

[63] J. Gobrecht, Schwereseigerungen von Eisen, Mangan und Chrom in Aluminium-Silicium-Gußlegierungen (Teil 1), Giesserei 62 (1975) 263–266.

[64] J.L. Jorstad, Understanding ``Sludge'', Die Cast Eng. 30 (1986) 30–36.

[65] R. Dunn, Aluminum melting problems and their influence on furnace selection, Die Cast Eng. B 9 (1965) 8–30.

[66] G. Timelli, S. Capuzzi, A. Fabrizi, Precipitation of primary Fe-rich compounds in secondary AlSi9Cu3(Fe) alloys, J. Them. Anal. Calorim. 123 (2016) 249–262.

[67] M. Makhlouf, D. Apelian: Casting Characteristics of aluminum die cast alloys, Work performed under contract No. DEFC07-99ID13716 prepared for US department of energy office of industrial technologies prepared by the advanced casting research center Worcester Polytechnic Institute, 2002, pp. 1–46.

[68] D. Ferdian, C. Josse, P. Nguyen, N. Gey, N. Ratel-Ramond, P. de Parseval, Y. Thebault, B. Malard, J. Lacaze, L. Salvo, Chinese script vs plate-like precipitation of beta-$Al_9Fe_2Si_2$ phase in an Al-6.5Si-1Fe alloy, Metall. Mater. Trans. A 46 (2015) 2814–2818.

[69] B.G. Dietrich, H. Becker, M. Smolka, A. Keβler, A. Leineweber, G. Wolf, Intermetallic sludge formation in Fe containing secondary Al–Si alloys influenced by Cr and Mn as preparative tool for metal melt filtration, Adv. Eng. Mater. 19 (2017) 1–7, 1700161.

[70] H. l. de Moares, J.R. de Oliveira, D.C.R. Espinosa, J.A.S. Tenório, Removal of iron from molten recycled aluminum through intermediate phase filtration, Mater. Trans. 47 (2006) 1731–1736.

[71] H.M. Van der Donk, G.H. Nijhof: U.S. Patent, 5741348, "Method for refining an aluminum scrap melt", 1998, date of filing 28.5.1996, grant of the patent 21.4.1998.

[72] A. Pisch, C. Kräutlein, P. Le Brun, G. Rombach, P. de Vries, M. Ryckeboer, C.J. Simensen, New experimental approach in the search of intermetallic compounds for Fe, Mn and Si removal in aluminum recycling, Light Metals (2005) 1191–1195, TMS., USA, 2005.

[73] A. Flores-V, M. Sukiennik, A.H. Castillejos-E., F.A. Acosta-G., J.C. Escobedo-B., A kinetic study on the nucleation and growth of the Al8FeMnSi2 intermetallic compound for aluminum scrap purification, Intermetallics, 6 (1998) 217–27.

[74] P. Ashtari, K. Tetley-Gerard, K. Sadayappan, Removal of iron from recycled aluminum alloys, Can. Metall. Quart. 51 (2012) 75–80.

[75] S.W. Kim, U.H. Im, H.C. Cha, S.H. Kim, J.E. Jang, K.Y. Kim, Removal of primary iron rich phase from aluminum-silicon melt by centrifugal separation, Ch. Foundry 10 (2013) 112–117.